Fully Metallic Luneburg Metalens Antenna in Gap Waveguide Technology at V-Band

Dayan Perez-Quintana, Christos Bilitos, Jorge Ruiz-Garcia, Inigo Ederra, Jorge Teniente-Vallinas, David Gonzalez-Ovejero, Miguel Beruete

Fully Metallic Luneburg Metalens Antenna in Gap Waveguide Technology at V-Band

Dayan Pérez-Quintana, Christos Bilitos, Jorge Ruiz-García, Iñigo Ederra, Jorge Teniente-Vallinas, David González-Ovejero, Miguel Beruete

***Abstract*— This paper presents the design of a flat Luneburg metalens antenna at V-band using Gap Waveguide (GW) technology. The metalens consists of a parallel plate waveguide loaded with metallic pins whose height is modulated to get an effective refractive index that follows the Luneburg equation. A Groove Gap Waveguide (GGW) H-plane horn is used to illuminate the metalens, such that the rays are collimated and a planar wavefront is generated in the direction of propagation. Since the structure at hand is planar, it can be efficiently integrated on flat surfaces. Moreover, the fully metallic structure is mechanically robust and presents lower losses than lenses including dielectric substrates. A prototype has been fabricated and tested, simulations and experimental results are in very good agreement. The metalens yields an input reflection coefficient (S_{11}) below -10 dB from 45 to 70 GHz, whereas the -3dB gain fractional bandwidth is 26.2% with respect to a center frequency of 60 GHz, with a peak of 22.5 dB at 61 GHz. These features make this design an interesting solution for millimeter-wave applications.**

***Index Terms*—Luneburg lens, gap waveguide technology, millimeter-waves, metalens, metasurface.**

I. Introduction

Wireless communication systems are in constant evolution, with each new standard defining higher data rates in order to satisfy the demands of a hyperconnected society. The race for data rate along with the saturation of the microwave spectrum are driving the exploration of higher frequency bands, which can provide broader bandwidths able to cope with these requirements. The millimeter-wave (MMW) band (from 30 to 300 GHz) can fulfill this purpose, since it allows for wide channelization bandwidths that fit the specifications of the fifth-generation (5G) and the incoming sixth-generation (6G) mobile communication systems [1]. Nevertheless, there remain some challenges that must be addressed to fully exploit all the potential of MMW in wireless communication technologies. For instance, highly directive antennas are needed to compensate for the increased free-space propagation loss compared to microwaves (due to the higher carrier frequencies) as well as additional losses due to atmospheric absorption.

Several solutions have been proposed to tackle these issues, including antenna arrays and reflector antennas with high directivity and good scanning performance [2], [3]. Despite being a feasible solution, antenna arrays need complex feeding networks, which lead to increased losses jeopardizing its practical applicability at MMW. Regarding reflector antennas, although cost-effective, the designs are bulky and require a mechanical steering of the complete antenna assembly.

Lens antennas have emerged in recent years as an alternative for wireless devices at high frequencies due to the high directivity and scanning resolution they offer with relatively simple structures [4]–[7]. Although lens antennas can be bulky at microwaves, they become more compact when scaled at MMW. One of the most versatile solutions is the Luneburg lens (LL) [8], whose rotationally symmetric graded index (GRIN) profile transforms a spherical wave into a planar wavefront with perfect impedance matching to free space. In turn, flat LLs [5], [7] collimate cylindrical wavefronts to radiate a fan beam.

The spatially varying refractive index in such lenses can be synthesized using metasurfaces and metamaterials with hybrid metallodielectric [5], [7], [9], [10] or fully metallic unit cells [11]–[15]. For example, metallodielectric Luneburg lenses (LL) were implemented in [5] and [9] by modulating the surface impedance inside a parallel-plate structure. However, the use of dielectrics is not recommendable at MMW due to the dielectric losses which, in some cases, can be high [16]. To avoid this limitation, fully metallic LL devices have been proposed. The multibeam LL antennas in [12] and [13] yielded good results using a bed of nails (metallic pins) with varying height to modulate the refractive index. To simplify the manufacturing process, a bed of nails with homogenous pin height was proposed in [11], and the refractive index modulation was implemented by varying the height of the metallic plate

Manuscript received XX; revised XX; accepted XX. Date of publication XX; date of current version XX. This work was supported This work was supported by MCIN/AEI/10.13039/ 501100011033/FEDER "Una manera de hacer Europa" via Project No. RTI2018-094475-B-I00. (Corresponding author: Miguel Beruete.)

Dayan Pérez-Quintana, Iñigo Ederra, Jorge Teniente and Miguel Beruete are with the Antennas Group, Universidad Pública de Navarra, 31006 Pamplona, Spain, and also with the Institute of Smart Cities (ISC), Universidad Pública de Navarra, 31006 Pamplona, Spain (e-mail: dayan.perez@unavarra.es; inigo.ederra@unavarra.es; jorge.teniente@unavarra.es; miguel.beruete@unavarra.es).

Christos Bilitos and David González-Ovejero are with Univ Rennes, CNRS, IETR (Institut d'Électronique et des Technologies du numéRique), UMR 6164, F-35000 Rennes, France.

Jorge Ruiz García is with the Electrical Engineering and Computer Science Department, University of Michigan, Ann Arbor, MI 48109 USA.

Color versions of one or more of the figures in this communication are available online at https://ieeexplore.ieee.org. Digital Object Identifier XXXX

opposite to the bed of nails.

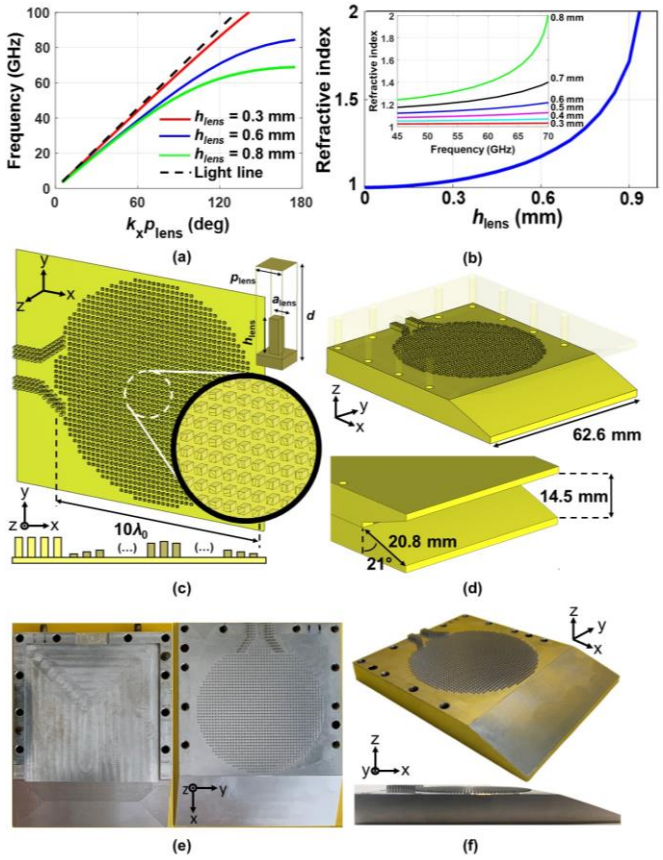

Fig. 1. (a) Dispersion diagram of a periodic metal pin structure for LL [shown in the inset of panel (c)] with the following dimensions: p_{lens} = 1.1 mm, a_{lens}= 0.5 mm and h_{lens} varying from 0.3 to 0.8 mm. (b) Equivalent refractive index as function of pin height at f_0 = 60 GHz. (Inset) Equivalent refractive index as a function of frequency for different pin heights (from 0.3 to 0.8 mm). (c) Schematic showing the LL and the GGW horn antenna; (top inset) zoom into the pins of the metalens in the central region; (bottom inset) sketch showing the metalens side view and pin schematic with main dimensions. (d) Perspective view of the bottom plate (top panel) and a zoom into the flared section (bottom panel). (e) Picture of the fabricated antenna showing a top view of the upper block (left) and bottom block (right) with the metalens horn antenna. (f) Photograph of the bottom piece in perspective view (top) and profile view (bottom) to show clearly both the lens and GGW antenna pins.

Another obstacle that must be circumvented to fully develop MMW technology resides in effectively guiding waves in closed structures. Typical solutions that perform well at microwaves, such as standard metallic waveguides, become more and more challenging as the frequency approaches the MMW band. At these frequencies, strict tolerances are required to get a good electrical contact and, hence, avoid additional losses. Respecting such tolerances by typical fabrication technologies might be difficult or have an excessive cost. A promising alternative at MMW is the Gap Waveguide (GW) technology, developed during the last decade to give a satisfactory technological response to this question [17]. GW has three main variants: groove-gap waveguide (GGW) [18], ridge-gap waveguide (RGW) [19] and microstrip-gap waveguide (MGW) [20]. In its most general configuration, GW technology uses a couple of bed of nails instead of lateral metallic walls. The pins' dimensions are selected to create a propagation bandgap, which confines the wave propagation within the volume delimited by the bed of nails and a couple of conducting plates on the top and bottom. A relevant feature of this technology is that electric contact between the top plate and the bed of nails is not required, so tolerances can be coarser alleviating the manufacturing constraints and, hence, its cost. In addition, losses at MMW are lower compared with standard rectangular waveguides and it is easily adaptable to flat surfaces [21].

In this article, we exploit the benefits of GGW technology to design and experimentally demonstrate a fully metallic flat LL antenna at 60 GHz, which is above the operation frequency of most LL-based antennas found in the literature. The LL is synthesized using metallic pins with variable height to implement the target refractive index profile. The LL is excited by a GGW horn antenna, whose phase center is placed at the focus of the metasurface LL. The proposed structure can be easily integrated with more ports to provide scanning capabilities with a fan beam radiation pattern. The experimental results show an excellent impedance matching and directivity in the entire operating bandwidth with a good agreement with the numerical simulations. The overall good performance of the device demonstrates that standard fabrication techniques are still valid at high frequencies where tolerances are stringent and the manufacturing of small details is challenging. This article builds upon our prior work in [22], [23], by presenting a more detailed design, comprehensive manufacturing and experimental demonstration of a metalens based on metallic pins with variable height.

II. Luneburg Lens Antenna Design

As mentioned in the introduction, a fully metallic design is implemented to avoid the loss of typical dielectric substrates in the MMW range, as well as to let the antenna withstand harsh environmental conditions. As explained in [5], it is possible to modulate the effective refractive index for a transverse magnetic (TM) surface wave by loading a parallel plate waveguide with a bed of nails consisting of metallic posts of different heights. The refractive index profile of a LL obeys the following equation:

$$n(r) = \sqrt{2 - \left(\frac{r}{R}\right)^2} \qquad (1)$$

where r is the radial distance between a point inside the lens and its center, and R is the external radius of the lens. In our design we consider a planar LL which radiates a fan beam.

The design of both the GRIN LL lens and the GGW horn antenna was carried out using the commercial simulator CST Microwave Studio® [24]. Aluminum was considered for all of the constituent pieces and was modeled as a lossy metal with a conductivity of 1.72×10^7 S/m [25].

Since the height variation between neighboring pins inside the lens is smooth, each pin can be considered as immersed in a locally periodic environment. Such local periodicity entitles one to treat each pin as a unit-cell in a periodic problem. Therefore, the dispersion characteristics for each unit-cell can be obtained in a straightforward manner by employing CST's

eigenmode solver. For instance, Fig. 1(a) shows the dispersion curves obtained for 3 different pin heights, h_{lens}. Using these curves, one can construct maps that link, for a specific frequency, the pin height to the wavenumber k_x of the fundamental TM mode inside the loaded PPW. The effective refractive index n_{eff} can, thus, be retrieved using $k_x = n_{eff} k_0$, as shown in Fig. 1(b) and inset.

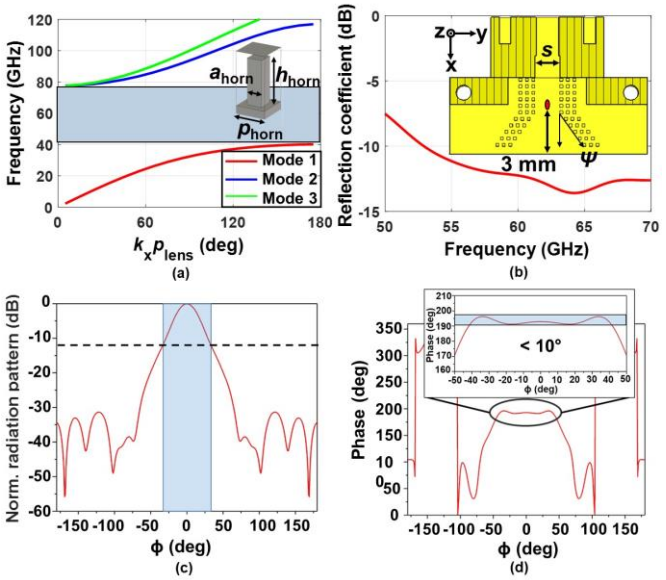

Fig. 2. (a) Dispersion diagram of a periodic metallic pin structure (shown in the inset) for GGW horn with dimensions: p_{horn} = 1 mm, a_{horn} = 0.5 mm and h_{horn} = 1.5 mm. (b) Simulated input reflection coefficient of the GGW horn antenna in dB; (inset) top view showing the width of the step (s=4.2 mm) the horn flare angle (Ψ=35°) and an estimation of the phase center. (c) Normalized magnitude of the H-plane radiation pattern at 60 GHz (simulation result); the shaded region is the angular aperture where the directivity is above −12 dB from the maximum (d) Phase of the H-plane radiation pattern at 60 GHz (simulation result); (inset) detail showing the phase variation in the ±50° range with the region where the phase variation is below 10° highlighted.

The GRIN LL is synthesized by dividing the circular area according to a Cartesian lattice that matches the selected periodicity, p_{lens}, of the unit-cell. Then, (1) is applied to compute the ideal refractive index in each square of the lattice. Such values can be mapped to a pin height (h_{lens}) using the curve depicted in the inset of Fig. 1(b). Fig. 1(c) shows the structure resulting of this synthesis process. The lens has an external diameter of 50 mm ($10\lambda_0$, where λ_0 is the free space wavelength at the design frequency f_0 = 60 GHz) and the metallic pin height varies between 0.3 and 0.8 mm. A flare section is implemented to improve the radiation pattern and the matching to free space, as shown in Fig. 1(d) and its inset. The PPW opens gradually with an angle of 21°, and its length is 20.8 mm. The height and width are 14.5×62.6 mm^2 and, hence, the physical aperture area is 907 mm^2.

The next step is to design the GGW horn antenna feeding the LL. It must be ensured that the wave is confined within the groove of width 4.2 mm and height 1.75 mm by the metallic pins and the top and bottom metallic plates. Again, the eigenmode solver of CST Studio Suite® was employed to obtain the pin dimensions that fix a bandgap around the operation frequency. As shown in Fig. 2(a), with a width of a_{horn} = 0.5 mm, a height of h_{horn} = 1.5 mm, periodicity p_{horn} = 1 mm and distance to the upper metallic layer of 0.25 mm, a bandgap arises centered at 60 GHz and spanning from 40 to 80 GHz.

Using these dimensions for the GGW pins, the H-plane horn was designed by gradually opening the waveguide with a linear variation and an angle of ψ = 35° for operation at 60 GHz. To emulate the experimental setup, the GGW was connected to a standard WR-15 waveguide. As the WR-15 waveguide and the GGW have different widths, a step transition was designed to avoid impedance mismatch. Fig 2(b) shows that the input reflection coefficient is below −10 dB from 54 GHz up to the upper limit of V band (70 GHz). The inset in Fig. 2(b) shows a top cross section view of the antenna highlighting the designed step s = 4.2 mm.

To optimize the performance of the lens-antenna system, the focus of the lens (which in an ideal LL should be exactly at the circumference) must be carefully aligned with the phase center of the GGW horn antenna. The phase center is determined from the simulation results of the H-plane at 60 GHz. First, we determine the angular aperture where the directivity decreases around −12 dB from its maximum value and find that it is ±42°, see Fig. 2(c). This value ensures a correct illumination of the lens without excessive spillover. Next, the phase center is found by searching a phase curve between these angles as flat as possible, Fig 2(d). After this process, it is concluded that the phase center is inside the GGW horn at 3 mm from the aperture, as depicted in the inset of Fig. 2(b). As shown in Fig 2(d), a small variation lower than 10° is achieved between ±42°.

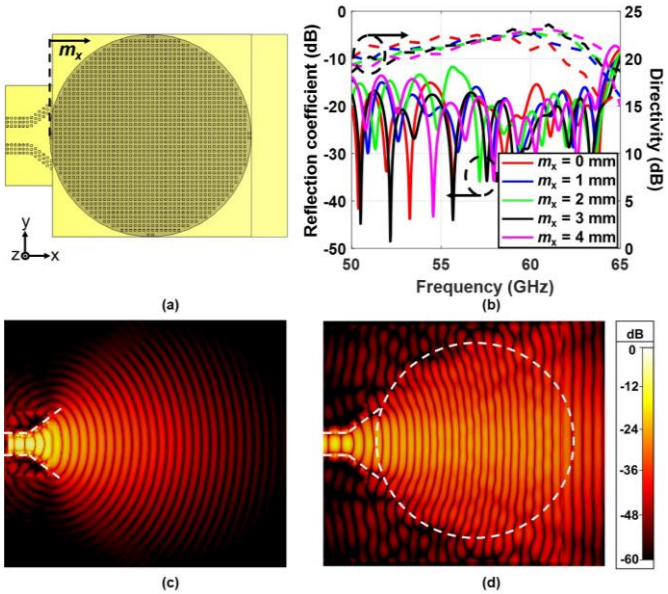

Fig. 3. (a) Schematic of LL, GGW horn antenna and flare (top view) highlighting the parameter m_x that controls the relative position of the lens and the horn antenna. (b) Parametric simulation results of reflection coefficient and directivity varying m_x from 0 to 4 mm. (c) Normalized $|E_z|$ without metalens at 60 GHz in decibel scale. (d) Normalized $|E_z|$ at 60 GHz with metalens in logarithmic scale.

The GGW horn antenna is therefore slightly inserted into the LL, as shown in Fig 1(c), to match the LL focal circumference with the horn's phase center. This is corroborated by a parametric analysis using an auxiliary parameter m_x, which represents how much the antenna is inserted inside the lens (m_x = 0 means that the antenna aperture coincides with the LL

focal circumference and a positive m_x means that the horn goes into the lens). Fig. 3(b) shows the reflection coefficient and directivity for several m_x varying from 0 to 4 mm. When the GGW horn aperture is exactly at the rim of the lens (m_x = 0 mm), the directivity drops at the upper frequency limit. The maximum directivity over the bandwidth is achieved when m_x = 3 mm, in good agreement with the phase center position previously calculated.

Finally, Fig. 3(c) and (d) show the top view of the normalized vertical component of the simulated electric field at 60 GHz with and without the lens. It is clear that the lens shapes the cylindrical wavefront radiated by the GGW horn into a planar wavefront. After all the design steps, the system has a total volume of 88.5×62.6×19.05 mm^3, see Fig. 1(e) and (f).

III. Prototype Fabrication and Result Analysis

The previously discussed LL GGW antenna was manufactured and measured. A standard computer numerical control (CNC) milling machining with a tolerance of ± 20 μm was selected to manufacture the two blocks in Fig. 1. As mentioned above, the material employed was aluminum due to its good conductivity and mechanical properties. Photographs of the manufactured prototype are shown in Fig. 1(e) and (f).

The far-field measurements were performed using two different setups. Radiation pattern planes, peak directivity and aperture efficiency (η_{eff}) were obtained using the planar near field setup shown in Fig. 4(a). In this setup, the lens antenna (Antenna Under Test, AUT) was aligned with its H-plane parallel to the *z*-axis and the E-plane parallel to the *y*-axis, see Fig. 4(a). An open-ended waveguide probe with sharp edges (surrounded with TK-RAM absorbing material to reduce undesired reflections [26]) was used to scan the electric field at a distance d_m = 70 mm from the AUT, far enough to prevent reactive coupling between the AUT and the probe and close enough to avoid measuring a very large plane. The measurements were taken by moving the probe position along the *yz*-plane in a rectangle of 560×240 mm^2 with a step of 2 mm (less than $\lambda_0/2$) and sweeping the frequency at each point. A precise alignment process was done to ensure that the AUT and the probe were parallel prior to recording the co-polar and cross-polar planar near fields. A PNA network analyzer E8361C (Agilent Technologies) was used to measure the antenna in the frequency range from 45 to 70 GHz, with the frequency span discretized in steps of 50 MHz. A single-port calibration was performed to measure the reflection coefficient of the lens antenna system. The far field radiation patterns and, from them, the directivity and aperture efficiency were finally obtained by applying a near to far field transformation and probe correction.

In addition, a far field setup was implemented to measure the gain by applying the gain comparison (or gain transfer) method [27], see Fig. 4(b). Two identical calibrated standard horn antennas (source and detector) of known gain and linear polarization were carefully aligned and placed at a distance of 2000 mm, farther than the minimum far field distance determined by the AUT dimensions, which is around 1930 mm at the maximum frequency of the band (70 GHz). To avoid undesired reflections on the ground between the antennas, the floor was covered with RAM. Nevertheless, the setup does not use an anechoic chamber and hence is prone to reflections with the objects in the laboratory, introducing some ripple and uncertainty in the measurements, at it will be shown below. The measurements were performed using an AB Millimetre Vector Network Analyzer MVNA-8-350 operating from 45 to 70 GHz with a frequency step of 0.5 GHz

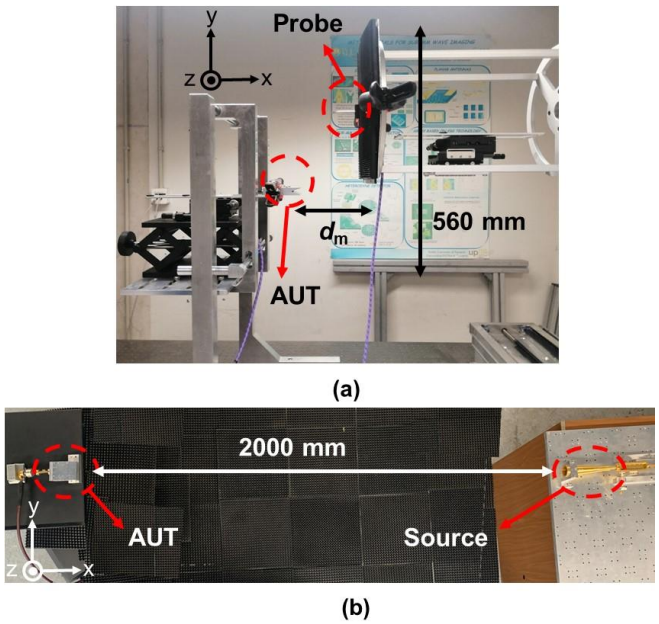

Fig. 4. Experimental setups used to characterize the AUT. (a) Near field setup highlighting the distance between the AUT and the probe (d_m = 70 mm); red circles mark the LL antenna (AUT) and the probe positions. (b) Far field setup (top view) highlighting the distance between the AUT and the source horn antenna of 2000 mm.

Fig. 5(a) shows the simulated (dashed) and experimental (solid) results corresponding to the magnitude of the input reflection coefficient (red) and the realized gain (blue) of the lens antenna. The antenna has a good impedance matching in all the considered band (from 45 to 70 GHz), with a reflection coefficient below −10 dB and an excellent agreement between simulation and experimental results. The experimental realized gain reaches a maximum value of 22.5 dB at 61 GHz and is above 20 dB in almost all the band, with a fair agreement with the simulation results. Furthermore, the realized gain bandwidth (defined as the frequency range where the gain is above –3 dB with respect to the maximum) is close to 15.7 GHz (from 50.7 GHz to 66.4 GHz). Hence, the fractional bandwidth is around 26.2%.

Fig. 5(b) shows the measured directivity (blue curve) and aperture efficiency (η_{eff}, green curve). Notice that the realized gain and directivity have similar values thanks to the fully metallic design that has low ohmic loss. Indeed, the numerically simulated radiation efficiency reaches a high value of 96.8%. Nevertheless, experimental values of the gain must be taken with some caution since there are some regions where the it is above the experimental directivity, a result that is obviously unphysical. These happen due to the mentioned measurement uncertainties of the far field setup. Hence, it is not possible to

retrieve the experimental radiation efficiency from these measurements. The aperture efficiency, extracted from the directivity, is between 0.2 and 0.3 from 50 to 65 GHz and decreases at higher frequencies, see Fig. 5(b). This parameter could be improved with a different flare implementation aimed at reducing the E-plane beamwidth by following a different shape such as an exponential curve for example [28]. Nevertheless, given that antennas with a fan-beam pattern like the one considered here usually have moderate values of aperture efficiency (as a result of the wide beamwidth in one of the radiation planes) a linear flare was chosen in the design to simplify the manufacturing process.

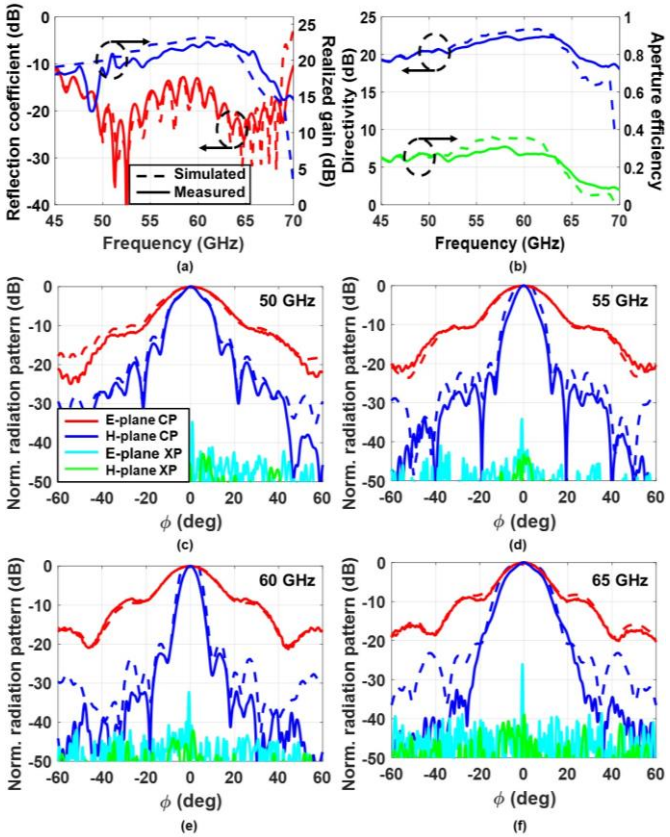

Fig. 5. Simulated (dashed lines) and measured (solid lines) results of several antenna parameters. (a) Reflection coefficient (red) and realized gain (blue) versus frequency in dB. (b) Directivity (blue curve) versus frequency response in dB and aperture efficiency (η_{eff}) from 45 to 70 GHz (green curve). Normalized far field radiation patterns at: (c) 50 GHz, (d) 55 GHz, (e) 60 GHz and (f) 65 GHz.

The co-polar and cross-polar radiation patterns are shown in Fig. 5(c)-(f). Radiation patterns are only represented from $-60° \leq \theta \leq 60°$. This limitation comes from the size of the sampled plane along with the AUT size and the distance between the AUT and the probe, which do not allow to obtain larger angles with the applied near-field setup method. To illustrate the antenna performance, several representative frequencies were selected and plotted (from 50 to 65 GHz with steps of 5 GHz). The E-plane (co-polar in red and cross-polar in cyan) and H-plane (co-polar in blue and cross-polar in green) normalized radiation patterns are included in all cases. Again, an excellent agreement between simulation and experimental results is observed. Obviously, the antenna presents a narrower beamwidth in H-plane than in E-plane (at 60 GHz, $H_{HPBW} = 6.8°$ and $E_{HPBW} = 21°$), since the former one is the plane where the LL collimates the beam. The side lobe level at 60 GHz is around −22 dB and in the worst case is −15 dB at 50 GHz. An excellent cross-polar discrimination, higher than 25 dB, is noticed in all cases.

There are nevertheless some experimental results that need further clarification. First, there is a dip in the measured directivity between 55 and 60 GHz that does not appear in the simulation results [Fig. 5(b)]. Furthermore, this dip is in apparent contradiction with the behavior observed in the radiation patterns, where the beamwidth in the measured H-plane is narrower than in the simulation [Fig. 5(d), (e)]. However, looking closely, it can be observed that the measured E-plane is wider and has higher side lobes, counterweighting the beamwidth reduction in the H-plane and leading to a decrease of the measured directivity in that frequency range. This phenomenon can be attributed to very small errors in the manufactured prototype.

In addition to this, there is an important directivity drop at 65 GHz that appears both in the simulation and experimental results. This is a consequence of the dispersion of the metallic pin array used to modulate the refractive index by varying the pin height as presented in Fig. 1(a). From that figure and also from Fig. 1(b), it is clear that the refractive index is dispersive and has an abrupt variation from 65 GHz onwards, especially for pin heights between 0.7 and 0.8 mm. To fully understand the underlying physics, the discretization applied to modulate the LL must also be considered. A contour plot of the ideal refractive index distribution applying (1) is presented in Fig. 6(a), where a small discretization step of 0.1 mm has been employed. However, the implemented lens has a coarser period ($p_{lens} = 1.1$ mm) leading to the discretized index profile shown in Fig. 6(b). Gray circles superimposed in that figure delimit the boundaries of regions of pins with the same height (up to 22 different pin heights were used in the lens). Looking closely, it is found that most of the lens area (up to 48.1%) contains pins with heights above 0.7 mm, which have strong dispersion above 65 GHz. Therefore, it can be concluded that the drop in directivity beyond this frequency is a consequence of the pin dispersion, which leads to refractive index values far from the Luneburg equation. This is corroborated in Figs. 6(c) and (d) that show the electric field distribution at 65 and 70 GHz. It is appreciated that the field inside the lens greatly differs from the electric field when the refractive index matches the Luneburg equation [Fig. 3(d)]. Hence, the output wavefront is no longer planar and this effect leads to the observed directivity drop.

There are excellent works in the literature that propose metamaterial unit cells with low dispersion [7], [12], [29]. For instance, some implementations such as glide symmetric unit cell designs are less dispersive, giving rise to wide bandwidth and good directivity performances. However, this technology is difficult to implement as frequency increases due to the small gap between lower and upper pins needed to obtain wide bandwidth.

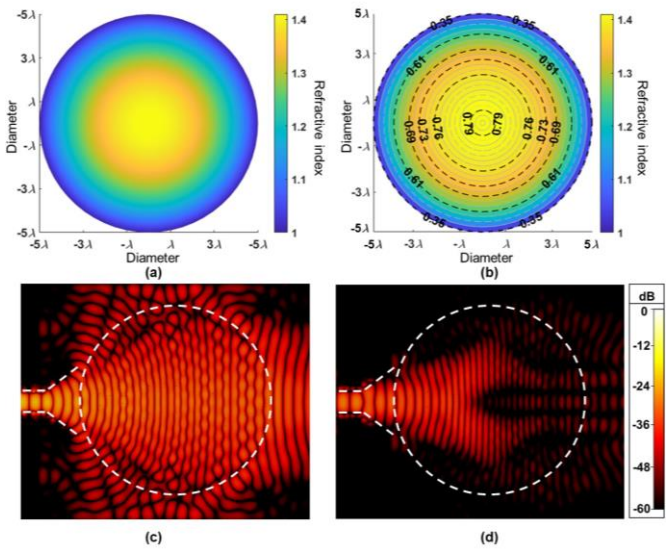

Fig. 6. (a) Planar LL and its radially symmetric refractive index n(r) with a discretization of 0.1 mm. (b) Mapping representation of the LL refractive index implemented with discretization of $p_{lens} = 1.1$ mm, where the gray dashed circles delimit the regions with pins of the same height (black dashed circles are some selected labels). (c) Top view of the normalized $|E_z|$ metalens in decibel scale at 65 GHz. (d) Idem at 70 GHz.

All the antenna results, both numerical and experimental, are summarized in Table I.

TABLE I
COMPARISON BETWEEN SIMULATED AND MEASURED RESULTS

Parameter	Simulated	Measured
S11 (dB) BW*	50-65 GHz	50-65 GHz
Peak Gain	23.2 dB at 61 GHz	22.5 dB at 61 GHz
Fractional Gain BW+	24.8%	26.2%
SLL (at 60 GHz)	20 dB	22.4 dB
HPBW (at 60 GHz)	E-plane = 21° H-plane = 7°	E-plane = 21° H-plane = 6.8°

* Defined as the bandwidth where S11 < −10 dB. Total BW is in GHz.
+ Defined as the bandwidth where the directivity is reduced by 3 dB with respect to the maximum, divided by the frequency of maximum directivity.

IV. CONCLUSION

To conclude, we have demonstrated a fully metallic LL antenna system excited by a GGW horn operating at V-band. The LL has been synthesized using metallic pins to obtain the desired refractive index profile, which provides a planar wavefront in the direction of propagation. A GGW horn antenna has been also designed and combined with the LL to get a fully metallic design compatible with the requirements of wireless communication systems at MMW. Owing to the fully metallic design, this system is more robust and presents lower losses than solutions involving typical dielectric substrates. Moreover, the final design is flat, making it easy to adapt to planar surfaces. The simulated and experimental results are in good agreement, demonstrating that CNC micromachining is a viable manufacturing alternative even at high frequencies where tolerances are critical and designs based on small constituents such as metallic pins are challenging. A peak realized gain of 22.5 dB is achieved at 61 GHz, with a gain bandwidth of around 26.2%. A cross-polarization discrimination higher than 25 dB is observed in the measured bandwidth. The physical behavior of the antenna has been analyzed in detail to understand the performance worsening beyond 65 GHz. It has been concluded that it is a consequence of the bed of nails dispersion, which is especially critical for pin heights from 0.7 to 0.8 mm that form a 48.1% of the total area of the lens. This antenna based on GGW technology is able to generate excellent radiation characteristics and could be used in applications at MMW.

ACKNOWLEDGEMENT

The authors are grateful to Laurent Cronier and Xavier Morvan (Université de Rennes 1 and IETR's M^{2}ARS platform) for the fabrication of the prototype.

REFERENCES

[1] H. Tataria, M. Shafi, A. F. Molisch, M. Dohler, H. Sjoland, and F. Tufvesson, "6G Wireless Systems: Vision, Requirements, Challenges, Insights, and Opportunities," *Proc. IEEE*, vol. 109, no. 7, pp. 1166–1199, Jul. 2021, doi: 10.1109/JPROC.2021.3061701.

[2] A. Dadgarpour, M. A. Antoniades, A. Sebak, A. A. Kishk, M. Sharifi Sorkherizi, and T. A. Denidni, "High-Gain 60 GHz Linear Antenna Array Loaded With Electric and Magnetic Metamaterial Resonators," *IEEE Trans. Antennas Propag.*, vol. 68, no. 5, pp. 3673–3684, May 2020, doi: 10.1109/TAP.2020.2964945.

[3] J. Li, C. Matos, and N. Ghalichechian, "A Low-Cost Vertically Integrated Antenna Array at 60 GHz With 85% Efficiency," *IEEE Antennas Wirel. Propag. Lett.*, vol. 20, no. 4, pp. 513–517, Apr. 2021, doi: 10.1109/LAWP.2021.3055726.

[4] W. Yuan *et al.*, "Glide-Symmetric Lens Antenna in Gap Waveguide Technology," *IEEE Trans. Antennas Propag.*, vol. 68, no. 4, pp. 2612–2620, Apr. 2020, doi: 10.1109/TAP.2019.2955919.

[5] M. Bosiljevac, M. Casaletti, F. Caminita, Z. Sipus, and S. Maci, "Non-Uniform Metasurface Luneburg Lens Antenna Design," *IEEE Trans. Antennas Propag.*, vol. 60, no. 9, pp. 4065–4073, Sep. 2012, doi: 10.1109/TAP.2012.2207047.

[6] O. Orgeira, G. Leon, N. J. G. Fonseca, P. Mongelos, and O. Quevedo-Teruel, "Near-Field Focusing Multibeam Geodesic Lens Antenna for Stable Aggregate Gain in Far-Field," *IEEE Trans. Antennas Propag.*, vol. 70, no. 5, pp. 3320–3328, May 2022, doi: 10.1109/TAP.2021.3139093.

[7] O. Zetterstrom, R. Hamarneh, and O. Quevedo-Teruel, "Experimental Validation of a Metasurface Luneburg Lens Antenna Implemented With Glide-Symmetric Substrate-Integrated Holes," *IEEE Antennas Wirel. Propag. Lett.*, vol. 20, no. 5, pp. 698–702, May 2021, doi: 10.1109/LAWP.2021.3060283.

[8] R. K. Luneburg, *Mathematical Theory of Optics*. University of California Press, 1964.

[9] J. Li *et al.*, "Design of a Broadband Metasurface Luneburg Lens for Full-Angle Operation," *IEEE Trans. Antennas Propag.*, vol. 67, no. 4, pp. 2442–2451, Apr. 2019, doi: 10.1109/TAP.2018.2889006.

[10] J. G. Marin and J. Hesselbarth, "Lens Antenna With Planar Focal Surface for Wide-Angle Beam-Steering Application," *IEEE Trans. Antennas Propag.*, vol. 67, no. 4, pp. 2757–2762, Apr. 2019, doi: 10.1109/TAP.2019.2894336.

[11] H. Lu, Z. Liu, J. Liu, G. Wu, Y. Liu, and X. Lv, "Fully Metallic Anisotropic Lens Crossover-in-Antenna Based on Parallel Plate Waveguide Loaded With Uniform Posts," *IEEE Trans. Antennas Propag.*, vol. 68, no. 7, pp. 5061–5070, Jul. 2020, doi: 10.1109/TAP.2020.2975261.

[12] O. Quevedo-Teruel, J. Miao, M. Mattsson, A. Algaba-Brazalez, M. Johansson, and L. Manholm, "Glide-Symmetric Fully Metallic Luneburg Lens for 5G Communications at Ka-Band," *IEEE Antennas Wirel. Propag. Lett.*, vol. 17, no. 9, pp. 1588–1592, Sep.

2018, doi: 10.1109/LAWP.2018.2856371.
[13] J. Liu, H. Lu, Z. Dong, Z. Liu, Y. Liu, and X. Lv, "Fully Metallic Dual-Polarized Luneburg Lens Antenna Based on Gradient Parallel Plate Waveguide Loaded With Nonuniform Nail," *IEEE Trans. Antennas Propag.*, vol. 70, no. 1, pp. 697–701, Jan. 2022, doi: 10.1109/TAP.2021.3098544.
[14] J. Ruiz-Garcia, E. Martini, C. Della Giovampaola, D. Gonzalez-Ovejero, and S. Maci, "Reflecting Luneburg Lenses," *IEEE Trans. Antennas Propag.*, vol. 69, no. 7, pp. 3924–3935, Jul. 2021, doi: 10.1109/TAP.2020.3044668.
[15] F. Fan, M. Cai, J. Zhang, Z. Yan, and J. Wu, "Wideband Low-Profile Luneburg Lens Based on a Glide-Symmetric Metasurface," *IEEE Access*, vol. 8, pp. 85698–85705, 2020, doi: 10.1109/ACCESS.2020.2992653.
[16] E. Rajo-Iglesias, M. Ferrando-Rocher, and A. U. Zaman, "Gap Waveguide Technology for Millimeter-Wave Antenna Systems," *IEEE Commun. Mag.*, vol. 56, no. 7, pp. 14–20, Jul. 2018, doi: 10.1109/MCOM.2018.1700998.
[17] P.-S. Kildal, E. Alfonso, A. Valero-Nogueira, and E. Rajo-Iglesias, "Local Metamaterial-Based Waveguides in Gaps Between Parallel Metal Plates," *IEEE Antennas Wirel. Propag. Lett.*, vol. 8, pp. 84–87, 2009, doi: 10.1109/LAWP.2008.2011147.
[18] A. Berenguer, V. Fusco, D. E. Zelenchuk, D. Sanchez-Escuderos, M. Baquero-Escudero, and V. E. Boria-Esbert, "Propagation Characteristics of Groove Gap Waveguide Below and Above Cutoff," *IEEE Trans. Microw. Theory Tech.*, vol. 64, no. 1, pp. 27–36, Jan. 2016, doi: 10.1109/TMTT.2015.2504501.
[19] D. Perez-Quintana, A. E. Torres-Garcia, I. Ederra, and M. Beruete, "Compact Groove Diamond Antenna in Gap Waveguide Technology With Broadband Circular Polarization at Millimeter Waves," *IEEE Trans. Antennas Propag.*, vol. 68, no. 8, pp. 5778–5783, Aug. 2020, doi: 10.1109/TAP.2020.2996364.
[20] J. Liu, A. Vosoogh, A. U. Zaman, and J. Yang, "Design and Fabrication of a High-Gain 60-GHz Cavity-Backed Slot Antenna Array Fed by Inverted Microstrip Gap Waveguide," *IEEE Trans. Antennas Propag.*, vol. 65, no. 4, pp. 2117–2122, Apr. 2017, doi: 10.1109/TAP.2017.2670509.
[21] Young-Jin Park, A. Herschlein, and W. Wiesbeck, "A photonic bandgap (PBG) structure for guiding and suppressing surface waves in millimeter-wave antennas," *IEEE Trans. Microw. Theory Tech.*, vol. 49, no. 10, pp. 1854–1859, 2001, doi: 10.1109/22.954798.
[22] D. Perez-Quintana, C. Bilitos, J. Ruiz-Garcia, D. Gonzalez-Ovejero, and M. Beruete, "Fully Metallic Luneburg Lens Antenna in Gap Waveguide Technology at 60 GHz," in *XXXVII Simposio Nacional de la Unión Científica Internacional de Radio (URSI 2022)*, 2022, p. 19.
[23] D. Perez-Quintana, C. Bilitos, J. Ruiz-Garcia, D. Gonzalez-Ovejero, and M. Beruete, "Flat Lens Antenna using Gap Waveguide Technology at Millimeter Waves," in *2021 Fifteenth International Congress on Artificial Materials for Novel Wave Phenomena (Metamaterials)*, Sep. 2021, pp. 343–346, doi: 10.1109/Metamaterials52332.2021.9577146.
[24] "CST STUDIO SUITE." https://www.3ds.com/products-services/simulia/products/cst-studio-suite.
[25] T. Strober, S. Tubau, E. Girard, H. Legay, G. Goussetis, and M. Ettorre, "Shaped Parallel-Plate Lens for Mechanical Wide-Angle Beam Steering," *IEEE Trans. Antennas Propag.*, vol. 69, no. 12, pp. 8158–8169, Dec. 2021, doi: 10.1109/TAP.2021.3090789.
[26] "TK-RAM absorbing material to reduce scattered fields." http://www.terahertz.co.uk/index.php?option=com_content&view=article&id=145&Itemid=448 (accessed January. 8, 2022).
[27] G. A. Hurd, "IEEE Standard Test Procedures for Antennas," *Electron. Power*, vol. 26, no. 9, p. 749, 1980, doi: 10.1049/ep.1980.0385.
[28] N. J. G. Fonseca, Q. Liao, and O. Quevedo-Teruel, "Equivalent Planar Lens Ray-Tracing Model to Design Modulated Geodesic Lenses Using Non-Euclidean Transformation Optics," *IEEE Trans. Antennas Propag.*, vol. 68, no. 5, pp. 3410–3422, May 2020, doi: 10.1109/TAP.2020.2963948.
[29] A. Arayeshnia and S. Amiri, "High-Efficiency Metallic Elliptical Lens Antenna Based on Glide-Symmetric Nails Bed," *IEEE Antennas Wirel. Propag. Lett.*, vol. 20, no. 7, pp. 1180–1184, Jul. 2021, doi: 10.1109/LAWP.2021.3074817.

Dayan Pérez-Quintana was born in Cuba in 1991. He received the degree in telecommunication engineering from the Instituto Superior Politécnico José Antonio Echeverría (ISPJAE), Havana, Cuba, in 2015 and the Ph.D. degree in Telecommunication Engineering from the Public University of Navarra (UPNA), Spain, in 2022. During his Ph.D. studies, he spent three months as Research Stay in the School of Electrical Engineering and Computer Science (EECS) at KTH Royal Institute of Technology, Stockholm, Sweden. He was working as a Pre-Doctoral Research Fellow with the Antenna Group, Electrical, Electronic and Communication Engineering Department, Public University of Navarre (UPNA), Pamplona, Spain, from 2018 to 2022. His interests include millimeter-wave and THz components and antennas and metamaterials.
Dr. Pérez-Quintana was a recipient of the Young Scientist Award at the at 3rd URSI Atlantic Radio Science Meeting (AT-AP-RASC) in 2022.

Christos Bilitos was born in Serres, Greece, in 1994. He received his M.S. degree in telecommunication engineering from Aristotle University of Thessaloniki, Thessaloniki, Greece, in April 2018.
From 2018 to 2020, he worked in industry before beginning his Ph.D. studies at the Institut d'Electronique et des Technologies du numéRique (IETR), Rennes, France in collaboration with the Agence Innovation Défense (AID). During the course of his Ph.D. studies, he spent four months as a visiting scholar at the University of Siena in 2021 and 2022.
His research interests include computational electromagnetics, leaky-wave structures, metasurfaces and GRIN lenses for mm-wave antennas.

Jorge Ruiz-García received the M.S. degree in telecommunication engineering from the Universidad de Granada, Granada, Spain, in 2015, and the Ph.D. degree in electronics from the Université de Rennes I, Rennes, France, in 2021. From 2022, he is a Postdoctoral Research Fellow with the Radiation Laboratory in the University of Michigan, Ann Arbor, MI, USA. He worked as an Intern at CREATIS-Lyon, Lyon, France, and in industry before joining the Institut d'Électronique et des Technologies du numéRique (IETR), Rennes, France, in 2017, to pursue his Ph.D. degree in collaboration with the Agence de l'Innovation de Défense (AID). He spent five months as a Visiting Scholar at the University of Siena, Siena, Italy, from 2019 to 2020. His research interests include metasurfaces, periodic structures, antennas, lenses, and beam-formers for microwave to submillimeter wave applications.

Dr. Ruiz-García was a recipient of the Best Paper Award in Electromagnetics at the 15th European Conference on Antennas and Propagation (EuCAP) in 2021.

Iñigo Ederra (M'15) received the M.Sc. and Ph.D. degrees in Telecomunication Engineering from the Universidad Pública de Navarra, Pamplona, Spain, in 1996 and 2004, respectively.

In 1997, he joined the Microwave and Millimetre Wave Group, Universidad Pública de Navarra. From 1999 to 2000 he was with the European Space Research and Technology Centre (ESTEC), ESA, Noordwijk, The Netherlands, where he was working on Electromagnetic Bandgap materials and their applications in the field of antennas. Since 2001 he is with the Antenna Group, Universidad Pública de Navarra. From June to October 2002 he was visitor scientist at the Rutherford Appleton Laboratory, Chilton, Didcot, UK, participating in ESA´s Startiger I project. Currently, he is a Full Professor at the Universidad Pública de Navarra and is a member of its Institute of Smart Cities.

His research interests are in the field of Metamaterials and Metasurfaces and their applications in microwave, millimetre wave and THz components and antennas.

Jorge Teniente was born in Lodosa, Navarra, Spain in 1973. He received the M.Sc. and Ph.D. degrees in Telecommunication Engineering from the Public University of Navarra (UPNA), Spain, in 1997 and 2003, respectively. Since 1997, he has been with the Antenna Group of the Public University of Navarra, where he is currently an Associate Professor and has been involved in the research activity of his research group. Between 1999 and 2000, he was a Spanish Trainee at ESA/ESTEC, Noordwijk, The Netherlands. In summer 2002, he was a Research Scientist at the ESA project "StarTiger 1" at Rutherford Appleton Laboratory in England, and from 2004 to 2005, he was at University of Oviedo, Asturias, Spain. Dr. Teniente received the 2nd prize award of the V Rosina Ribalta awards in 2003 and the Telefónica Foundation award at the XXIV awards of COIT and AEIT in 2004. During his research activity, Dr. Teniente has designed antennas for various satellites, radiometers, radio telescopes and various related applications for more than 25 years and he is a founding partner of the company ANTERAL S.L. which markets high-performance horn antennas for space and ground applications, low-cost radar products and components/technologies in the microwave, millimeter, submillimeter and THz frequency bands. His current area of research is in the field of horn antenna technology, OMTs, septums and polarizers and in design, manufacture and measurement of horn antennas in mm-wave, sub-mm-wave and THz frequencies as weel as fabrication of mm and submm-wave circuits at clean room environment.

David González-Ovejero (S'01–M'13–SM'17) received the M.S. degree in telecommunication engineering from the Universidad Politécnica de Valencia, Valencia, Spain, in 2005, and the Ph.D. degree in electrical engineering from the Université catholique de Louvain, Louvain-la-Neuve, Belgium, in 2012. From 2012 to 2014, he was a Research Associate with the University of Siena, Siena, Italy. In 2014, he joined the Jet Propulsion Laboratory, California Institute of Technology, Pasadena, CA, USA, where he was a Marie Curie Post-Doctoral Fellow. Since 2016, he has been a tenured researcher with the French National Center for Scientific Research (CNRS), Institut d'Electronique et des Technologies du numéRique (IETR), Rennes, France. His current research interests include computational electromagnetics, large phased arrays, periodic structures, metasurfaces and submillimeter wave antennas.

Dr. González-Ovejero was a recipient of a Marie Curie International Outgoing Fellowship from the European Commission in 2013, the Sergei A. Schelkunoff Transactions Prize Paper Award from the IEEE Antennas and Propagation Society in 2016, the Best Paper Award in Antenna Design and Applications at the 11th European Conference on Antennas and Propagation in 2017, and the Best Paper Award in Electromagnetics at the 15th European Conference on Antennas and Propagation in 2021. Since 2019, he has been an Associate Editor of the IEEE TRANSACTIONS ON ANTENNAS AND PROPAGATION and the IEEE TRANSACTIONS ON TERAHERTZ SCIENCE AND TECHNOLOGY.

Miguel Beruete received the M.Sc. and Ph.D. degrees in telecommunication engineering from the Public University of Navarre (UPNA), Pamplona, in 2002 and 2006, respectively. From 2007 to 2009, he was with the Electronics Department, Technological Center CEMITEC. In 2009, he joined TERALAB, UPNA, as a Post-Doctoral Researcher of the Consolider EMET Engineering Metamaterials Project. From 2012 to 2016, he was a Ramon y Cajal Fellow Researcher and in 2017 he was appointed UPNA Distinguished Researcher.

Since 2017, he is an Associate Professor in UPNA where he leads the TERALAB Laboratory. In 2018 he became group leader of the Multispectral Biosensing Group in Navarrabiomed. He has authored near 160 indexed articles, 5 book chapters, and more than 350 conference communications (several invited). He holds three patents and has participated in more than 70 research projects/contracts (PI in 22) of international, national and regional funding. His current research interests include metasurfaces and metamaterials for infrared applications (radiative cooling, camouflage, etc.) and millimeter/terahertz-wave communication technologies.

Dr. Beruete has been included in the Stanford University's list of the top 2% most-cited scientists in the world in three consecutive editions (2020, 2021, 2022), was awarded with the

Ph.D. Prize from UPNA for the Best Doctoral Thesis (2006 - 2007), the Research Prize UPNA for the best scientific contribution (2017 – 0218), three CST University Publication awards (2005, 2012, 2016), the XII Talgo Award of Technological Innovation in 2011, and several awards of international conferences. He is a reviewer for more than 50 international journals.